Astronomy & Astrophysics

Special issue

First polar observations of the fast solar wind with the Metis – Solar Orbiter coronagraph: Role of 2D turbulence energy dissipation in the wind acceleration

D. Telloni[1], E. Antonucci[1], L. Adhikari[2], G. P. Zank[2,3], S. Giordano[1], M. Vai[1], L.-L. Zhao[2], V. Andretta[4],
A. Burtovoi[5], G. E. Capuano[6,7], V. Da Deppo[8], Y. De Leo[9,7], S. Fineschi[1], C. Grimani[10,11], P. Heinzel[12,13],
G. Jerse[14], F. Landini[1], A. Liberatore[15], J. D. Moses[16], G. Naletto[17], G. Nicolini[1], M. Pancrazzi[1], M. Romoli[18],
G. Russano[4], C. Sasso[4], A. Slemer[8], D. Spadaro[6], M. Stangalini[19], R. Susino[1], L. Teriaca[9], M. Uslenghi[20],
L. Sorriso-Valvo[21,22], R. Marino[23], D. Perrone[19], R. D'Amicis[24], and R. Bruno[24]

(Affiliations can be found after the references)

ABSTRACT

Context. The fast solar wind is known to emanate from polar coronal holes.
Aims. This Letter reports the first estimate of the expansion rate of polar coronal flows performed by the Metis coronagraph on board Solar Orbiter.
Methods. By exploiting simultaneous measurements in polarized white light and ultraviolet intensity of the neutral hydrogen Lyman-α line, it was possible to extend observations of the outflow velocity of the main component of the solar wind from polar coronal holes out to $5.5\,R_\odot$, the limit of diagnostic applicability and observational capabilities.
Results. We complement the results obtained with analogous polar observations performed with the UltraViolet Coronagraph Spectrometer on board the SOlar and Heliospheric Observatory during the previous full solar activity cycle, and find them to be satisfactorily reproduced by a magnetohydrodynamic turbulence model.
Conclusions. This suggests that the dissipation of 2D turbulence energy is a viable mechanism for coronal plasma heating and the subsequent acceleration of the fast solar wind.

Key words. magnetohydrodynamics (MHD) – Sun: corona – solar wind – Sun: UV radiation

1. Introduction

Fifty years ago, the source of the ecliptic streams of fast solar wind detected in interplanetary space was identified, with a persistent large-scale X-ray feature discovered on the solar disk during a sounding rocket flight: a coronal hole extending in longitude from the northern to the southern polar cap, characterized by open magnetic field lines (Krieger et al. 1973). However, detection of the fast wind emanating directly from the core of polar coronal holes was only made possible in the declining and minimum phase of solar cycle 22 during the first polar orbit of Ulysses (Wenzel et al. 1992) around the Sun, when out-of-the-ecliptic exploration of the solar wind was carried out with the in situ Solar Wind Ion Composition Spectrometer (SWICS; Gloeckler et al. 1992) instrument, combined with the first observations of the coronal wind in the years 1996−1997 with the UltraViolet Coronagraph Spectrometer (UVCS; Kohl et al. 1995) on board the SOlar and Heliospheric Observatory (SOHO; Domingo et al. 1995). The fast wind, which has an expansion rate in interplanetary space of $\geq 700\,\mathrm{km\,s^{-1}}$ as measured with in situ instruments, was found to fill most of the solar minimum heliosphere (Woch et al. 1997; McComas et al. 1998) and corona (Dolei et al. 2018; Telloni 2021; Telloni et al. 2022a); whereas the slow wind, propagating in the heliosphere at about

$400\,\mathrm{km\,s^{-1}}$, was confined to a region about $\pm 30°$ wide around the equator. These results have been confirmed by interplanetary scintillation data collected over two solar cycles, which indicate that during solar minima the fast wind is strongly predominant in high-latitude regions above $\pm 70°$ from the equator (Tokumaru et al. 2010). According to UVCS observations, the hydrogen component of the solar wind reaches a velocity of $\geq 300\,\mathrm{km\,s^{-1}}$ at $3.1-3.5\,R_\odot$ in the core of polar coronal holes (Kohl et al. 1998; Cranmer et al. 1999; Antonucci et al. 2000; Dolei et al. 2018). We refer the reader to Cranmer (2020) for an extensive comparison of observational and model results.

The Metis coronagraph (Fineschi et al. 2020; Antonucci et al. 2020) on board Solar Orbiter (Müller 2020), launched on February 10, 2020, was designed to continue the detection begun with UVCS of the neutral hydrogen flow, and provides an opportunity to study the corona in a solar minimum configuration quite similar to that observed with SOHO and Ulysses on the previous full solar activity cycle. During the instrument commissioning phase, Metis first imaged the coronal wind on the entire plane of the sky (POS) as it propagated across a corona shaped by a typical solar minimum magnetic dipole. This included a detailed map from 3.8 to $7.0\,R_\odot$ of the equatorial $\pm 30°$ slow solar wind (Romoli et al. 2021), consisting of an accelerating low-speed stream along the coronal current sheet and two
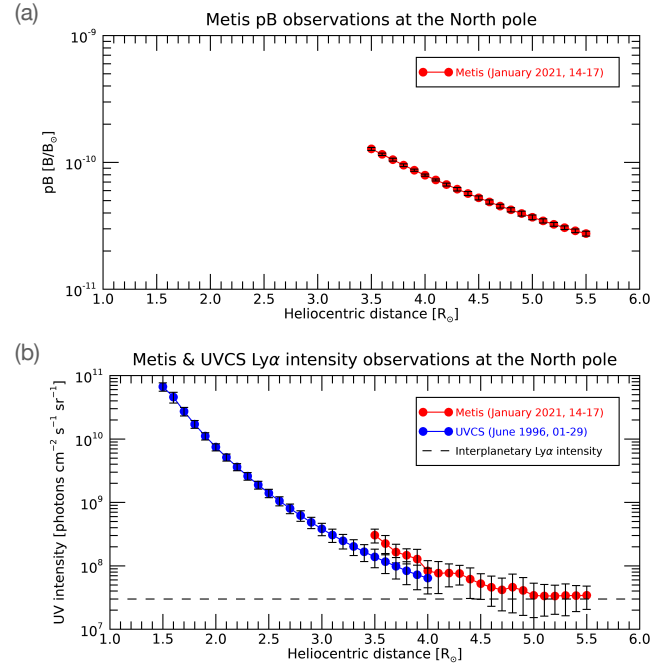
surrounding high-velocity sheared layers (Antonucci et al. 2022). By exploiting quadrature observations between Metis and the Parker Solar Probe (PSP; Fox et al. 2016), Telloni et al. (2021, 2022b) first studied the evolution of the ecliptic slow coronal flows to the very inner heliosphere in their transition from a sub-Alfvénic to super-Alfvénic regime.

The goal of this Letter is to analyze high-latitude coronal regions imaged by Metis in order to derive the speed of the fast wind emerging from the polar coronal hole and complement the UVCS solar minimum data, thus extending, for the first time in the literature, observations of the proton component flow from 1.9 out to $5.5\,R_\odot$. The results obtained from the combined analysis of UVCS and Metis data are compared with a magnetohydrodynamic (MHD) model based on solar wind and turbulence transport equations, in the framework of the nearly incompressible (NI) MHD theory (Zank et al. 2017, 2018, 2020), with the aim being to cast more light on the processes that accelerate the fast solar wind.

2. Observations

From January 14 through January 17, 2021, Metis acquired 23 pairs of images in polarized brightness (pB) and in the ultraviolet (UV) light band centered on the neutral hydrogen H I Lyman-α spectral line. The observed field of view (FOV) extends approximately from 3.5 to $6.3\,R_\odot$. The set of images was processed and calibrated in flight according to De Leo et al. (2023) and De Leo et al. (in prep.). To increase the signal-to-noise ratio in the very faint coronal hole regions, the 23 images were combined, taking care to account for the slightly different plate scale due to the approach of SO toward the Sun, from 0.61 to 0.58 au, during the Metis observations[1]. The merged data were then averaged in steps of $0.1\,R_\odot$ in a cone centered on the Sun's rotation axis of $60°$ in width above the north pole (consistent with the extension of polar coronal holes at solar minimum Woo et al. 1999). The resulting pB and UV radial profiles are shown, along with the relative uncertainties, as red dots in Figs. 1a and b, respectively, only up to $5.5\,R_\odot$, that is, up to where UV measurements are just above the interplanetary (i.e., noncoronal) contribution in the UV band observed by Metis (3×10^7 photons cm^{-2} s^{-1} sr^{-1}, Kohl et al. 1997, horizontal dashed line in Fig. 1b). This height therefore represents the observational limit for the detection of the UV Lyα corona.

Immediately evident is the greater noise level of the Metis UV observations compared with those in pB. In order to extend the UV profile to lower heights, down to $1.5\,R_\odot$ (blue dots in Fig. 1b), a similar averaging was performed over a full-corona map reconstructed from the UVCS synoptic observational program during Carrington rotation (CR) 1910 (i.e., from June 01 to 29, 1996). Even if the two datasets refer to periods 25 years apart, belonging to the activity minima of solar cycles 22 (UVCS) and 24 (Metis), the radial trends seem to reconcile relatively well (within uncertainties), although the intensities measured by Metis are slightly higher than those of UVCS in the range $3.5-4.0\,R_\odot$. As discussed below, in light of the fact that pB measurements also lead on average to higher electron densities than those typical in coronal holes during the 1996–1997 minimum, this suggests that the solar minimum corona conditions may have been slightly different, as expected because two

---

[1] In 4 days of observation, the Carrington longitude spanned more than $40°$, which means that different structures crossing the POS may have been averaged together. However, this is not critical in spherically symmetric polar coronal holes.

Fig. 1. pB (a) and UV (b) radial profiles at the north polar coronal hole, as measured by Metis (red dots) and UVCS (blue dots). The horizontal dashed line indicates the interplanetary H I Lyα intensity.

different solar cycles are compared, one in pre-minimum phase (UVCS) and the other in post-minimum phase (Metis).

3. Analysis

The H I Lyα line emission is dominated by resonant scattering of the disk radiation because the contribution from free-electron collisions is negligible due to the very rarefied solar atmosphere. Specifically, photons from the Sun's lower atmosphere are absorbed by neutral hydrogen atoms, leading the electron to make a quantum jump from the ground state ($n = 1$, where n is the principal quantum number) to the immediately higher energy level ($n = 2$). The subsequent spontaneous (2p–1s) transition to the fundamental level produces the H I Lyα line at $\lambda_0 = 121.6$ nm. Incident photons distribute around λ_0 according to the chromospheric profile. Similarly, the velocity distribution function of hydrogen atoms sets the coronal absorption profile. The resonance between the incident and absorption profiles determines the intensity of the emitted H I Lyα line. As hydrogen atoms expand outwardly, the incoming radiation is Doppler-shifted (toward red, i.e., longer wavelengths) in the rest frame of the scattering atoms, reducing this resonance and causing a dimming in the Lyα emission. This effect is known as Doppler dimming (Withbroe et al. 1982; Noci et al. 1987). If the outflow velocity of emitting atoms is sufficiently high, excitation and absorption profiles are completely Doppler-shifted, the scattered radiation totally dimmed, and the corona becomes invisible at the wavelength of 121.6 nm. As a result, observations of the UV solar corona and, particularly, measurements of the intensity of the H I Lyα, can be used to probe the speed of the expanding coronal plasma. Indeed, in the regions below approximately $10\,R_\odot$, where the time for hydrogen-proton charge exchange is less than the coronal expansion time (see, e.g., Withbroe et al. 1982), the neutral hydrogen flow traces that of protons, which are the species carrying most of the mass of the solar wind and thus represent the main component of the coronal plasma.

More specifically, the intensity of the radiatively excited H I Lyα line is given by

$$I_{\mathrm{r}} = \frac{B_{12}h\nu_0}{4\pi} \int_{-\infty}^{+\infty} n_{\mathrm{H}}\mathrm{d}l \int_{\Omega} p(\varphi)\mathrm{d}\omega \int_0^{\infty} I_{\mathrm{ex}}(\nu - \delta\nu)\phi(\nu)\mathrm{d}\nu, \quad (1)$$

where B_{12} is the Einstein coefficient for absorption, h the Planck constant, ν_0 the rest frequency, n_{H} the number density of the emitting hydrogen atoms, I_{ex} and ϕ the chromospheric radiation and coronal absorbing profiles, respectively, and $\delta\nu$ is their frequency shift in the frame of reference of the expanding solar wind. $p(\varphi)$ describes the scattering process geometry (Noci et al. 1987), where φ is the angle between the directions of the incident photon before and after scattering with hydrogen atoms. Integrals are computed along the line of sight (LOS) and on the solid angle Ω subtended by the solar disk at the scattering point, respectively. In particular,

$$n_{\mathrm{H}} = \frac{n_{\mathrm{H}}}{n_{\mathrm{p}}}\frac{n_{\mathrm{p}}}{n_{\mathrm{e}}}n_{\mathrm{e}}, \quad (2)$$

where $R(T_{\mathrm{e}}) = n_{\mathrm{H}}/n_{\mathrm{p}}$ is the ionization balance (a function of the electron temperature T_{e}, Arnaud & Rothenflug 1985) and $n_{\mathrm{p}}/n_{\mathrm{e}}$ is the ratio between proton and electron number densities (which depends on the elemental composition of the coronal plasma). Specifically, considering a fully ionized plasma with 90% hydrogen and 10% helium yields $n_{\mathrm{p}}/n_{\mathrm{e}} = 0.83$. If the helium abundance reduces to 5%, $n_{\mathrm{p}}/n_{\mathrm{e}} = 0.91$. Finally, the coronal absorption profile is defined by the local microscopic motion of the hydrogen atoms, that is, their kinetic temperature, parallel ($T_{\parallel}$) and perpendicular ($T_{\perp}$) to the magnetic field. It follows that the H I Lyα line intensity is a function of the electron density n_{e} and temperature T_{e}, the helium abundance A_{He}, the intensity of the lower atmosphere exciting radiation I_{ex}, hydrogen parallel ($T_{\parallel}$) and perpendicular ($T_{\perp}$) kinetic temperatures, and outflow velocity V_{out} (through $\delta\nu$): $I_{\mathrm{r}} = I_{\mathrm{r}}(n_{\mathrm{e}}, T_{\mathrm{e}}, A_{\mathrm{He}}, I_{\mathrm{ex}}, T_{\parallel}, T_{\perp}, V_{\mathrm{out}})$.

While the electron density n_{e} can be directly derived from the Metis pB measurements via the van de Hulst (1950) approach and the average chromospheric radiance at the time of the Metis observation (5.38×10^{15} photons cm^{-2} s^{-1} sr^{-1}) is provided by the LASP Interactive Solar Irradiance Data Center[2], all other coronal and chromospheric physical quantities are either based on previous estimates or are not known and some assumption is needed. Specifically, the analytic expression of the Lyα chromospheric profile is given by Auchère (2005). Three different radial profiles of electron temperature in coronal holes were considered in the analysis: two come from Guhathakurta et al. (1999) and Vásquez et al. (2003), while a third was derived so as to be compatible at low heights with the measurements reported by David et al. (1998) and at large distances from the Sun with the temperatures typically observed in high-speed streams at 1 au ($\sim 10^5$ K, Schwenn & Marsch 1990). The helium abundance, largely unknown in coronal holes, was assumed to be 5% or 10%. Information on the kinetic temperature of hydrogen atoms in polar holes stems from extensive UVCS measurements. The component along the LOS (and thus perpendicular to the magnetic field lines) was derived from the width of the H I Lyα spectral line as observed by UVCS. Measurements reported by Dolei et al. (2016) from 1.3 to 3.7 $R_{\odot}$ were extrapolated in the range of interest of the present analysis using the functional form given by Vásquez et al. (2003). Finally, as far as the par-

---

(a)

(b)
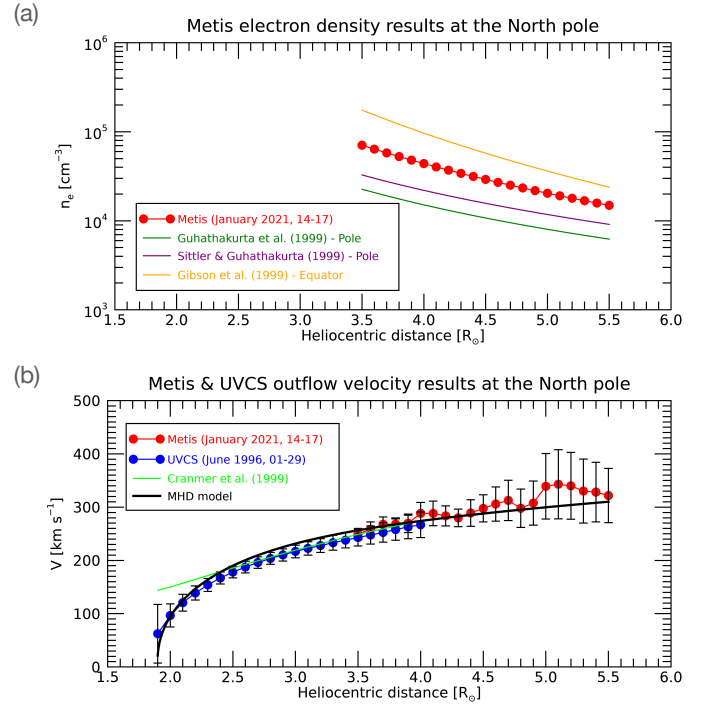
Fig. 2. n_{e} (a) and V_{out} (b) radial profiles at the north polar coronal hole, as measured with Metis (red dots) and UVCS (blue dots) data, compared with some results from previous literature (marked with different colored lines, as listed in the legend). The thick solid black curve in panel (b) denotes the NI MHD turbulence + SW model applied to the joint UVCS – Metis V_{out} estimates.

allel component is concerned, UVCS observations revealed that in the regions where the coronal wind is accelerating, the velocity distribution of the hydrogen atoms becomes anisotropic, that is, with larger values across the magnetic field than along it, above 2.2 $R_{\odot}$ (Kohl et al. 1998). Therefore, in this study, a maximum temperature anisotropy, $T_{\parallel} = T_{\mathrm{e}}$, is assumed. The only parameter still unknown or assumed, that is, the coronal plasma outflow velocity, can therefore now be inferred from Metis measurements.

4. Results

The electron density n_{e} at the north pole –inferred from Metis by inverting the pB radial profile of Fig. 1a (van de Hulst 1950)– is displayed in Fig. 2a, where it is compared with reference estimates at the poles (Guhathakurta et al. 1999; Sittler & Guhathakurta 1999) and along equatorial streamers (Gibson et al. 1999).

As mentioned above, the electron density is found to be slightly higher ($\sim 1.5-2$ times) than is typical for coronal holes at the minimum activity of solar cycle 22 (Guhathakurta et al. 1999; Sittler & Guhathakurta 1999), albeit still lower than the values corresponding to equatorial streamers (Gibson et al. 1999), which can be considered as an upper limit. However, it is also worth noting that the trend is similar and, in particular, the density scales as r^{-2} (where r is the heliocentric distance) far from the Sun, as expected. A similar increase in UV Lyα intensity with respect to UVCS observations is noted in Sect. 2. Given the independence of these measurements, this strongly suggests that the polar solar corona is slightly denser than in the previous full activity cycle.

Figure 2b shows the coronal wind speed derived with Metis (red dots) and UVCS[3] (blue dots) observations following the diagnostics outlined in Sect. 3. Speed estimates are not reliable below $1.9\,R_\odot$, being $\ll 100\,\mathrm{km\,s^{-1}}$: indeed, the Doppler dimming analysis of the H I Lyα line is applicable in a limited outflow velocity range from about 100 to $350\,\mathrm{km\,s^{-1}}$ (see, e.g., Withbroe et al. 1982). Therefore, only the UVCS – Metis velocity values from 1.9 to $5.5\,R_\odot$ are displayed in Fig. 2b. This is also the range where the coronal signal is measurable (at $5.5\,R_\odot$, it is just above the interplanetary contribution; see Fig. 1a). That is, the range of distances shown in the figure corresponds to the limits of current diagnostic and observational capabilities. The error bars account for both the uncertainties related to the UV measurements and the different assumptions of electron temperature and helium abundance considered in the analysis. The lower-altitude UVCS estimates and the higher-altitude Metis estimates match very well in the range where the measurements of the two instruments overlap ($3.5–4.0\,R_\odot$), showing a reasonably uniform radial profile as a whole. This shows that, regardless of the different coronal conditions, the expansion rate of the coronal plasma appears to be a characteristic parameter of the solar minimum corona, suggesting that the processes that accelerate the wind must have a degree of regularity over time through solar cycles. The acceleration rate is greater below $2.0−2.4\,R_\odot$, and beyond that, protons flow roughly with the same acceleration rate up to $5−5.5\,R_\odot$. Indeed, the coronal wind speed increases rapidly from $<100\,\mathrm{km\,s^{-1}}$ at $1.9\,R_\odot$ to about $170\,\mathrm{km\,s^{-1}}$ at $2.4\,R_\odot$, and then gradually increases with distance to $300−350\,\mathrm{km\,s^{-1}}$ at $5.0−5.5\,R_\odot$. However, it is evident that further acceleration, roughly constant at $\sim 0.02\,\mathrm{km\,s^{-2}}$, persists at higher distances (as is expected and required to explain the $\geq 700\,\mathrm{km\,s^{-1}}$ velocity of fast wind streams measured in interplanetary space; see, e.g., Schwenn & Marsch 1990). We also note the good agreement between the present results and those obtained by Cranmer et al. (1999) (green line in Fig. 2b) for distances above $2.4\,R_\odot$, although the two radial profiles diverge significantly lower down. This may be due to differences in the values of the parameters adopted in the diagnostics, and in the integration along the LOS (not taken into account by Cranmer et al. 1999), the correct estimation of which becomes increasingly important closer to the Sun.

The observed evolution of the corona expansion rate has been compared with the NI MHD theory in the context of quasi-2D turbulence, using the fast solar wind turbulence model developed by Zank et al. (2018) and Adhikari et al. (2020). In the NI MHD description, 2D turbulence is dominant over slab turbulence (Zank & Matthaeus 1992a,b, 1993). Zank et al. (2017) and Zank et al. (2018) first successfully applied the NI MHD theory to the study of turbulence in the super-Alfvénic solar wind and solar corona, respectively. Adhikari et al. (2020) then developed an NI MHD turbulence-driven + solar wind (SW) model for a high-speed plasma flow emerging from an open coronal hole, finding good agreement between theoretical predictions and PSP measurements. Later, Telloni et al. (2022a) extended it to include super-radial expansion (see also Adhikari et al. 2022) and a turbulent shear source in order to describe the increased correlation between temperature and outflow velocity observed

Table 1. NI MHD turbulence + SW model boundary conditions.

2D	Values	Slab	Values
$\langle z^{\infty +2}\rangle$ [km^2 s^{-2}]	3×10^5	$\langle z^{*+2}\rangle$ [km^2 s^{-2}]	2×10^4
$\langle z^{\infty -2}\rangle$ [km^2 s^{-2}]	3×10^5	–	–
E_D^∞ [km^2 s^{-2}]	2×10^3	–	–
λ_∞^+ [km]	8×10^4	λ_*^+ [km]	1.6×10^5
λ_∞^- [km]	8×10^4	–	–
$\lambda_\mathrm{D}^\infty$ [km]	8×10^4	–	–

Notes. Boundary values for turbulence quantities (outward and inward Elsässer energies $\langle z^{\pm 2}\rangle$ and the corresponding correlation lengths $\lambda^\pm$, residual energy E_D and the corresponding correlation length λ_D) at $1.9\,R_\odot$. The superscripts "∞" and "$*$" denote 2D and slab component, respectively.

at the interface between fast and slow coronal flows and interpreted in terms of Kelvin-Helmholtz instability. In the present analysis, the 1D steady-state NI MHD turbulence + SW model developed by Telloni et al. (2022a) and Adhikari et al. (2022) is used; it consists of six 2D turbulence transport equations, two slab turbulence transport equations, and three solar wind equations (continuity, momentum, and pressure). However, as the region of interest is the core of polar coronal holes, where shear effects are negligible (if any), the turbulent shear source is neglected here.

Using solar wind boundary conditions consistent with the results found here –or the assumptions previously adopted– and the turbulence boundary conditions shown in Table 1, the 1D steady-state NI MHD turbulence + SW model is numerically solved by the Runge-Kutta fourth-order method. In the model, 60% of the dissipated turbulence energy is assumed to heat the solar corona[4]. The hot coronal plasma generates a large pressure gradient, which drives the solar wind to become supersonic. As shown in Fig. 2b, the UVCS – Metis findings are remarkably well reproduced by the model (thick solid black line) over the whole range of observed distances. Interestingly, the outflow velocity increases rapidly up to the sonic point (located for the present observations around $2.0−2.4\,R_\odot$, depending on the electron temperatures considered; in this regard, see also Telloni et al. 2019), which is related to the rapid dissipation of 2D turbulence energy (see Zank et al. 2018; Adhikari et al. 2020). Beyond the sonic point, the 2D turbulence energy decreases gradually with distance, reducing the rate of effective wind acceleration.

The striking agreement between observations and theory is important for two reasons. First, it is an observational validation of the Adhikari et al. (2020) model (and the NI MHD theory in general Zank et al. 2017, 2018, 2020), which has mostly been tested against in situ heliospheric measurements. Second, it sheds light on the processes that accelerate the fast wind in open-field coronal holes, pointing to turbulence as a viable mechanism for the heating and subsequent acceleration of coronal plasma.

5. Conclusions

The combined observations of UVCS and Metis, although relative to two different magnetic cycles, made it possible, for the first time, to trace the propagation of the fast wind proton flow

---

[3] The same assumptions adopted for Metis were also used for UVCS, except for the electron density (not directly available from UVCS data, and so the estimates by Guhathakurta et al. 1999, which are representative of the solar minimum polar coronal hole, were employed) and the average chromospheric intensity (=5.33×10^{15} photons cm^{-2} s^{-1} sr^{-1} for CR 1910).

[4] It should be noted that the boundary conditions of 2D and slab turbulence energy and related correlation length (which controls the dissipation rate of the turbulence energy) may influence the modeled coronal speed.

from 1.9 out to $5.5\,R_\odot$, where speeds of $300-350\,\mathrm{km\,s^{-1}}$ are reached, de facto extending the observational range to the limit of diagnostic applicability. The agreement between the observations and a turbulence-driven NI MHD model strongly suggests that the dissipation of quasi-2D turbulence (created by the magnetic carpet and transported into the solar corona) can account for coronal heating and wind acceleration.

A further important point can be made about the rapid acceleration within $\sim 2.4\,R_\odot$. Because the NI MHD ($\beta \ll 1$, $\beta \sim 1$) model is dominated by 2D structures that are advected by the coronal flow, and because 2D flux ropes and magnetic islands dissipate and heat the coronal plasma by turbulent reconnection, much of the dissipation and heating will occur low in the solar atmosphere. Hence, rapid heating and rapid acceleration of the solar wind is an important feature of the NI MHD turbulence-driven model of the solar wind. Conversely, the Alfvén turbulence and wave-driven model of coronal heating and solar wind acceleration relies on the generation of inwardly propagating Alfvén waves created by reflection of the large-scale gradient of the expanding solar corona (Matthaeus et al. 1999; Verdini et al. 2009, 2010). Hence, coronal heating via the Alfvén turbulence model must occur on the expansion scale of the coronal hole, which is defined by the height of the Alfvén surface, that is, where the solar wind speed equals that of Alfvén waves ($\sim 9-11\,R_\odot$). This more gradual acceleration is in contrast with the initial rapid acceleration illustrated in Fig. 2 and is a distinguishing feature from the turbulence model of coronal heating. It is further worth noting that recent PSP observations presented by Bale et al. (2022) show rapid small-scale reconnection and associated heating very low in the coronal, which is consistent with the NI MHD turbulence model and the observation of rapid solar wind acceleration reported in this Letter.

References

Adhikari, L., Zank, G. P., & Zhao, L. L. 2020, ApJ, 901, 102
Adhikari, L., Zank, G. P., Telloni, D., & Zhao, L. L. 2022, ApJ, 937, L29
Antonucci, E., Dodero, M. A., & Giordano, S. 2000, Sol. Phys., 197, 115
Antonucci, E., Romoli, M., Andretta, V., et al. 2020, A&A, 642, A10
Antonucci, E., Downs, C., Capuano, G. E., et al. 2022, Phys. Fluids, submitted
Arnaud, M., & Rothenflug, R. 1985, A&AS, 60, 425
Auchère, F. 2005, ApJ, 622, 737
Bale, S. D., Drake, J. F., McManus, M. D., et al. 2022, ArXiv e-prints [arXiv:2208.07932]
Cranmer, S. R. 2020, ApJ, 900, 105
Cranmer, S. R., Kohl, J. L., Noci, G., et al. 1999, ApJ, 511, 481
David, C., Gabriel, A. H., Bely-Dubau, F., et al. 1998, A&A, 336, L90
De Leo, Y., Burtovoi, A., Teriaca, L., et al. 2023, A&A, submitted
Dolei, S., Spadaro, D., & Ventura, R. 2016, A&A, 592, A137
Dolei, S., Susino, R., Sasso, C., et al. 2018, A&A, 612, A84
Domingo, V., Fleck, B., & Poland, A. I. 1995, Sol. Phys., 162, 1
Fineschi, S., Naletto, G., Romoli, M., et al. 2020, Exp. Astron., 49, 239
Fox, N. J., Velli, M. C., Bale, S. D., et al. 2016, Space Sci. Rev., 204, 7
Gibson, S. E., Fludra, A., Bagenal, F., et al. 1999, J. Geophys. Res.: Space Phys., 104, 9691

Gloeckler, G., Geiss, J., Balsiger, H., et al. 1992, A&AS, 92, 267
Guhathakurta, M., Fludra, A., Gibson, S. E., Biesecker, D., & Fisher, R. 1999, J. Geophys. Res.: Space Phys., 104, 9801
Kohl, J. L., Esser, R., Gardner, L. D., et al. 1995, Sol. Phys., 162, 313
Kohl, J. L., Noci, G., Antonucci, E., et al. 1997, Sol. Phys., 175, 613
Kohl, J. L., Noci, G., Antonucci, E., et al. 1998, ApJ, 501, L127
Krieger, A. S., Timothy, A. F., & Roelof, E. C. 1973, Sol. Phys., 29, 505
Matthaeus, W. H., Zank, G. P., Oughton, S., Mullan, D. J., & Dmitruk, P. 1999, ApJ, 523, L93
McComas, D. J., Bame, S. J., Barraclough, B. L., et al. 1998, Geophys. Res. Lett., 25, 1
Müller, D., St. Cyr, O. C., Zouganelis, I., , et al. 2020, A&A, 642, A1
Noci, G., Kohl, J. L., & Withbroe, G. L. 1987, ApJ, 315, 706
Romoli, M., Antonucci, E., Andretta, V., et al. 2021, A&A, 656, A32
Schwenn, R., & Marsch, E. 1990, Physics of the Inner Heliosphere. I. Large-Scale Phenomena (Berlin, Heidelberg: Springer)
Sittler, E. C. Jr., & Guhathakurta, M. 1999, ApJ, 523, 812
Telloni, D. 2021, Universe, 7, 507
Telloni, D., Giordano, S., & Antonucci, E. 2019, ApJ, 881, L36
Telloni, D., Andretta, V., Antonucci, E., et al. 2021, ApJ, 920, L14
Telloni, D., Adhikari, L., Zank, G. P., et al. 2022a, ApJ, 929, 98
Telloni, D., Zank, G. P., Sorriso-Valvo, L., et al. 2022b, Astrophys. J., 935, 112
Tokumaru, M., Kojima, M., & Fujiki, K. 2010, J. Geophys. Res.: Space Phys., 115, A04102
van de Hulst, H. C. 1950, Bull. Astron. Inst. Neth., 11, 135
Vásquez, A. M., van Ballegooijen, A. A., & Raymond, J. C. 2003, ApJ, 598, 1361
Verdini, A., Velli, M., & Buchlin, E. 2009, ApJ, 700, L39
Verdini, A., Velli, M., Matthaeus, W. H., Oughton, S., & Dmitruk, P. 2010, ApJ, 708, L116
Wenzel, K. P., Marsden, R. G., Page, D. E., & Smith, E. J. 1992, A&AS, 92, 207
Withbroe, G. L., Kohl, J. L., Weiser, H., & Munro, R. H. 1982, Space Sci. Rev., 33, 17
Woch, J., Axford, W. I., Mall, U., et al. 1997, Geophys. Res. Lett., 24, 2885
Woo, R., Habbal, S. R., Howard, R. A., & Korendyke, C. M. 1999, ApJ, 513, 961
Zank, G. P., & Matthaeus, W. H. 1992a, J. Plasma Phys., 48, 85
Zank, G. P., & Matthaeus, W. H. 1992b, J. Geophys. Res.: Space Phys., 97, 17189
Zank, G. P., & Matthaeus, W. H. 1993, Phys. Fluids A, 5, 257
Zank, G. P., Adhikari, L., Hunana, P., et al. 2017, ApJ, 835, 147
Zank, G. P., Adhikari, L., Hunana, P., et al. 2018, ApJ, 854, 32
Zank, G. P., Nakanotani, M., Zhao, L. L., Adhikari, L., & Telloni, D. 2020, ApJ, 900, 115

1 National Institute for Astrophysics, Astrophysical Observatory of Torino, Via Osservatorio 20, 10025 Pino Torinese, Italy
   e-mail: daniele.telloni@inaf.it
2 Center for Space Plasma and Aeronomic Research, University of Alabama in Huntsville, Huntsville, AL 35805, USA
3 Department of Space Science, University of Alabama in Huntsville, Huntsville, AL 35805, USA
4 National Institute for Astrophysics, Astronomical Observatory of Capodimonte, Salita Moiariello 16, 80131 Napoli, Italy
5 National Institute for Astrophysics, Astrophysical Observatory of Arcetri, Largo Enrico Fermi 5, 50125 Firenze, Italy
6 National Institute for Astrophysics, Astrophysical Observatory of Catania, Via Santa Sofia 78, 95123 Catania, Italy
7 University of Catania, Department of Physics and Astronomy, Via Santa Sofia 64, 95123 Catania, Italy
8 National Research Council, Institute for Photonics and Nanotechnologies, Via Trasea 7, 35131 Padova, Italy
9 Max Planck Institute for Solar System Research, Justus-von-Liebig-Weg 3, 37077 Göttingen, Germany
10 University of Urbino Carlo Bo, Department of Pure and Applied Sciences, Via Santa Chiara 27, 61029 Urbino, Italy
11 National Institute for Nuclear Physics, Section in Florence, Via Bruno Rossi 1, 50019 Sesto Fiorentino, Italy
12 Czech Academy of Sciences, Astronomical Institute, Fričova 298, 25165 Ondřejov, Czech Republic
13 University of Wrocław, Centre of Scientific Excellence – Solar and Stellar Activity, ul. Kopernika 11, 51-622 Wrocław, Poland

[14] National Institute for Astrophysics, Astronomical Observatory of Trieste, Località Basovizza 302, 34149 Trieste, Italy

[15] Jet Propulsion Laboratory, California Institute of Technology, Pasadena, CA 91109, USA

[16] National Aeronautics and Space Administration, Headquarters, Washington, DC 20546, USA

[17] University of Padua, Department of Physics and Astronomy, Via Francesco Marzolo 8, 35131 Padova, Italy

[18] University of Florence, Department of Physics and Astronomy, Via Giovanni Sansone 1, 50019 Sesto Fiorentino, Italy

[19] Italian Space Agency, Via del Politecnico snc, 00133 Roma, Italy

[20] National Institute for Astrophysics, Institute of Space Astrophysics and Cosmic Physics of Milan, Via Alfonso Corti 12, 20133 Milano, Italy

[21] National Research Council, Institute for the Science and Technology of Plasmas, Via Amendola 122/D, 70126 Bari, Italy

[22] Swedish Institute of Space Physics, Ångström Laboratory, Lägerhyddsvägen 1, 751 21 Uppsala, Sweden

[23] Université de Lyon, Centre National de la Recherche Scientifique, École Centrale de Lyon, Institut National des Sciences Appliquées de Lyon, Université Claude Bernard Lyon 1, Laboratoire de Mécanique des Fluides et d'Acoustique, 69134 Écully, France

[24] National Institute for Astrophysics, Institute for Space Astrophysics and Planetology, Via del Fosso del Cavaliere 100, 00133 Roma, Italy